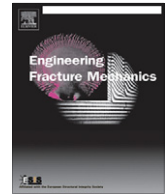




ELSEVIER

Contents lists available at SciVerse ScienceDirect

Engineering Fracture Mechanics

journal homepage: www.elsevier.com/locate/engfracmech

A rate-dependent homogenization based continuum plasticity-damage (HCPD) model for dendritic cast aluminum alloys

Piyush Dondeti^a, Daniel Paquet^a, Somnath Ghosh^{b,*}

^a Graduate Research Associate, The Ohio State University, United States

^b Michael G. Callas Professor, Departments of Civil and Mechanical Engineering, Johns Hopkins University, Baltimore, MD 21218, United States

ARTICLE INFO

Article history:

Received 21 November 2011

Received in revised form 31 March 2012

Accepted 10 April 2012

Keywords:

Anisotropic continuum plasticity damage model

Void nucleation

Viscoplasticity

GTN model

Void volume fraction

LE-VCFEM

ABSTRACT

This paper develops a rate-dependent homogenization based continuum plasticity damage model (HCPD) model for computationally efficient analysis of ductile failure in porous ductile materials containing brittle inclusions. The HCPD model developed has the overall structure of the anisotropic Gurson–Tvergaard–Needleman (GTN) model for porous ductile materials. The material is assumed to remain orthotropic in an evolving principal material coordinate system throughout the deformation history. The rate-dependency of plastic deformation is captured through an over-stress viscoplastic model. The anisotropic viscoplasticity parameters in the HCPD model depend on morphological features of the microstructure as well as on the plastic deformation. They are calibrated from homogenization of evolving micro-variables in a representative volume element (RVE) of the microstructure. Micromechanical analyses of the RVE are performed using the rate-dependent locally enhanced Voronoi cell finite element model (LE-VCFEM) [8,26]. This work also introduces a novel rate-dependent void nucleation criterion due to inclusion and matrix cracking in the underlying microstructure. Predictions of the rate-dependent HCPD model for a cast aluminum alloy are compared with the homogenized response obtained with LE-VCFEM micromechanical analyses of the actual microstructure with excellent agreement.

© 2012 Elsevier Ltd. All rights reserved.

1. Introduction

Metals and alloys in commercial application often contain heterogeneities like particulates, precipitates, intermetallics or voids in the microstructure. The micrograph of Al–Si–Mg hypoeutectic cast aluminum alloy W319, shown in Fig. 1, comprises age-hardened aluminum matrix, strengthened by Mg/Si and a dispersion of brittle Si particulates. The spatial distribution of the silicon particulates depends on the casting procedure and especially on the rate of heat extraction [15]. The solidification process pushes particulates into the regions between the evolving secondary dendrite arms. The heterogeneities often have adverse effects on failure properties like ductility of the overall material. Hence it is important to include the effects of morphology and distributions of heterogeneities in numerical models for deformation and failure. Cast alloys with small secondary dendrite arm spacing (SDAS) can be readily modeled using the locally enhanced Voronoi cell finite element model or LE-VCFEM developed by Ghosh et al. [8,20,26]. Alloys with large SDAS on the other hand can be modeled using a two-stage homogenization technique developed in [25]. The microscopic mechanisms leading to ductile failure in multi-phase materials such as cast aluminum alloys or discretely reinforced aluminum alloys (DRA) are void nucleation due to particle fragmentation and/or interface debonding, followed by void growth and coalescence within the matrix. Nucleation and

* Corresponding author. Tel.: +1 410 516 7833; fax: +1 410 516 7473.

E-mail address: sghosh20@jhu.edu (S. Ghosh).

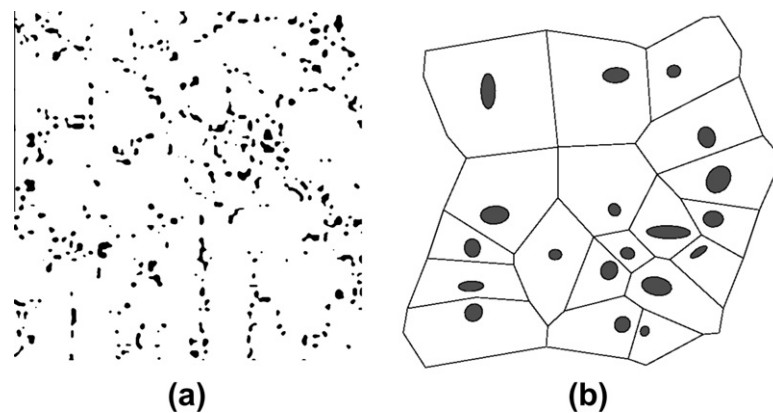


Fig. 1. (a) Micrograph of a cast aluminum alloy W319 ($192 \mu\text{m} \times 192 \mu\text{m}$), (b) RVE of the microstructure in (a) ($48 \mu\text{m} \times 48 \mu\text{m}$). This RVE is referred to as RVE 3.

growth of voids in the microstructure are very sensitive to the local morphological parameters and constitutive parameters [37]. It has been recently shown in [26] that damage evolution in the microstructure is also very sensitive to the strain rate.

The need for robust continuum (macroscopic) constitutive models, accounting for important morphological and material effects, is derived from the prohibitively large computational resources that would be required for large scale simulations with an explicit representation of each heterogeneity and their location in the microstructure. Various continuum constitutive models have been proposed for deformation and failure in heterogeneous materials based on phenomenological and micromechanical approaches. Many of the phenomenological models incorporate evolutionary variables that are formulated from experimental observations. However, their robustness is generally impaired by the lack of underlying mechanics and physics, as well as adequate microstructural representation. Alternatively, micromechanical models incorporate morphological details and solve boundary value problems of the representative volume element (RVE) to predict constitutive response at the macroscopic level. Such an RVE for the microstructure in Fig. 1a is shown in Fig. 1b. There are various analytical micromechanical models like those based on variational bounding methods, e.g. [38,29] and those based on effective medium approximations, e.g. [17,24]. These methods have limited capabilities for dealing with material nonlinearities, non-proportional load histories and complex morphologies. Multi-scale homogenization theories using asymptotic expansions and periodicity assumptions [2,31], for information transfer between macro- and micro-scales have been used for estimating averaged material properties of heterogeneous materials. Ghosh et al. [8,12–14] have implemented the asymptotic homogenization method with the micromechanical Voronoi cell finite element method (VCFEM) for multi-scale analysis of deformation and damage in nonuniformly dispersed microstructures. Micromechanical analysis that incorporate details of microstructural morphology, and deformation and failure mechanisms are computationally very expensive. Hierarchical models, such as the FE^2 multi-scale methods [6,5], on the other hand solve micro-mechanical RVE or unit cell models in every increment to obtain homogenized properties for macroscopic analysis. However, this method can be very expensive, as it entails solving the RVE micromechanical problem for every element integration point in the computational domain.

To overcome the shortcomings of prohibitive computational overhead, Ghosh et al. have developed the *homogenization based continuum plasticity-damage (HCPD)* model for heterogeneous materials undergoing ductile failure with evolving porosity [9]. The model represents the effect of morphological features and evolving microstructural mechanisms through evolving, anisotropic parameters. Parameters are established from homogenization of RVE response at microscopic scales. These reduced-order constitutive models are significantly more efficient than the FE^2 type models since they have limited information on microstructural morphology and do not have to solve the RVE problem in every step. The HCPD model is based on the Gurson–Tvergaard–Needleman or GTN model framework established in [16,4,34,35] that account for void nucleation, growth and coalescence. GTN models in which matrix anisotropy has been characterized by Hill's quadratic yield criterion have been proposed in [36,3]. Studies in [7] have shown that the yield surface of porous materials with rigid inclusions retain the form of the GTN yield surface.

The present paper extends the constitutive model proposed in [9] to account for rate dependent deformation and damage in heterogeneous metals and alloys. In [25], a rate-dependent homogenized over-stress viscoplasticity model has been developed for heterogeneous metals, but without any voids or damage. The present rate-dependent HCPD model introduces a novel damage evolution law. History dependence, resulting from local variations of the rate of deformation, is captured by the introduction of a new state variable quantifying the local fraction of cracked inclusion in the underlying microstructure. Calibration of the parameters in the rate-dependent HCPD model is performed by applying plane strain states of deformation on a 2D microstructure taken from a micrograph. While, it is acknowledged that a full 3D analysis would provide a more accurate representation of ductile fracture mechanisms in cast aluminum alloys, this paper is restricted to 2D analyses of inclusion and matrix cracking using the 2D LE-VCFEM discussed in Hu and Ghosh [20]. 2D analyses in Hu and Ghosh [20] have shown reasonably good agreement with experimental tests for microstructural deformation. Development of the rate-dependent HCPD model requires the following computational tools and procedures:

- (1) *Locally enhanced Voronoi cell FEM or LE-VCFEM*: All micromechanics simulations required for calibrating the rate-dependent HCPD model material parameters are done by LE-VCFEM [8,22,23,20]. It offers significant advantages in both efficiency and accuracy of micromechanical simulations for microstructures containing large number of heterogeneities. LE-VCFEM has been developed for viscoplastic materials in [26].
- (2) *RVE identification*: The size of the microstructural RVE or statistically equivalent RVE (SERVE) is an important parameter in the determination of homogenized microstructural properties. Various methods of identification of the SERVE, with and without damage, are described in [8,33,32,9]. A SERVE should be location independent in the microstructure in terms of yielding macroscopic response functions. Identification of the SERVE in this paper for a cast aluminum alloy W319 microstructure follows the method described in [9].
- (3) *Asymptotic expansion based homogenization (AEH)*: Development of the rate-dependent HCPD model requires evaluation of material parameters from homogenized stresses, strains and other state variables in the microstructural SERVE. The asymptotic expansion homogenization (AEH) method has been developed in [2,31] for homogenized constitutive models of heterogeneous materials. Ghosh et al. [8,13,14,30,10,7] have implemented the AEH method in conjunction with the micromechanical LE-VCFEM analysis. This is used in the development of this model.

The structure of the paper is as follows. The HCPD model is discussed for rate-dependent porous elastic–viscoplastic heterogeneous materials in Section 3. The procedure for calibration of the HCPD model material parameters is described in Section 4. Numerical examples and validations are presented in Section 5 for a computer simulated microstructural SERVE. Finally, the rate-dependent HCPD model is implemented in a macroscopic finite element analysis model and its predictive capabilities are assessed by comparing results with pure micromechanics simulations.

2. Micro-mechanical model and constitutive relations for individual phases

Micromechanical analysis of deformation and failure in heterogeneous materials, consisting of brittle inclusions in a ductile matrix, is conducted using the locally enhanced Voronoi cell finite element model or LE-VCFEM developed in [8,26]. The inclusions in a 2D microstructural section are assumed to be elastic and undergoing brittle fracture, while the matrix is represented by a rate and pressure-dependent elasto-viscoplastic model for porous materials undergoing ductile failure. Details of the adaptive, locally enhanced, hybrid LE-VCFEM formulation that admits local softening due to damage of the microstructure are provided in [8,21,26].

The inclusion phase in each Voronoi cell element is assumed to be isotropic, linear elastic. Instantaneous cracking of the inclusion follows a Weibull distribution based initiation criterion in [8,26], where a crack initiates when the probability function P_{frag} at any point in the inclusion exceeds a critical value. The probability function is defined as:

$$P_{frag}(v, \sigma_1^c) = 1 - \exp \left[-\frac{v}{v_0} \left(\frac{\sigma_1^c}{\sigma_w} \right)^m \right] \quad (1)$$

where m and σ_w are the Weibull modulus and the characteristic strength respectively and v_0 is a reference volume that scales with the microstructure. The probability function incorporates the inclusion size v and the maximum principal stress σ_1^c in its interior. The critical probability is taken to be $P_{frag}^{cr} = 95\%$. If this criterion is met at a point, an elliptical crack is introduced, which instantaneously extends to the inclusion boundary and fragments it.

The matrix phase is modeled as a rate-dependent elastic–viscoplastic material containing microscopic voids. The constitutive equations are developed in [26] as a rate-dependent viscoplasticity extension of the conventional rate-independent Gurson–Tvergaard–Needleman (GTN) model in [4,35]. The total strain-rate is assumed to admit an additive decomposition into an elastic and viscoplastic part as:

$$\dot{\epsilon} = \dot{\epsilon}^e + \dot{\epsilon}^p \quad (2)$$

For small strains, the rate of Cauchy stress $\dot{\sigma}$ is related to the elastic part of the strain rate tensor as: $\dot{\sigma} = \mathbf{C}^e : \dot{\epsilon}^e$, where \mathbf{C}^e is the fourth order isotropic elasticity tensor. The viscoplastic behavior of the porous ductile matrix is governed by the GTN yield function as:

$$\phi^{vp} = \left(\frac{q}{\bar{\sigma}_M} \right)^2 + 2f^* q_1 \cosh \left(-\frac{3q_2 p}{2\bar{\sigma}_M} \right) - (1 + q_3 f^{*2}) = 0 \quad (3)$$

where $q = \sqrt{\frac{3}{2} \boldsymbol{\sigma}' : \boldsymbol{\sigma}'}$ and $p = -\frac{1}{3} \boldsymbol{\sigma} : \mathbf{I}$ are the Von-Mises equivalent stress and the hydrostatic pressure respectively, $\boldsymbol{\sigma}'$ is the deviatoric stress and q_1, q_2, q_3 are void growth related parameters. f^* is a function of the void volume fraction f that is expressed in Eq. (18). The subscript M is used to designate association with the pure matrix material without voids. Hence, $\bar{\sigma}_M$ denotes the equivalent stress acting in the pure underlying viscoplastic matrix without voids. Deformation in the matrix material is assumed to be governed by the over-stress model of [28], for which the viscoplastic strain-rate is expressed as [11]:

$$\dot{\epsilon}_M^p = \gamma \langle \Phi_M(F_M) \rangle \frac{\partial \bar{\sigma}_M / \partial \boldsymbol{\sigma}_M}{\| \partial \bar{\sigma}_M / \partial \boldsymbol{\sigma}_M \|} \quad (4)$$

Here γ is a temperature dependent viscosity coefficient and $\langle \cdot \rangle$ is the MacCauley operator. $\Phi_M(F_M)$ is a function of the over-stress F_M , which is a measure of excess stress over the rate-independent local yield strength σ_0 (an internal state variable). It is expressed as:

$$F_M = \bar{\sigma}_M - \sigma_0(W_p) \quad (5)$$

The viscoplastic strain rate in Eq. (4) follows the associated flow rule and hence satisfies normality and incompressibility conditions. Here W_p is the inelastic work and $\bar{\sigma}_M (= \sqrt{\frac{3}{2}} \sigma'_M : \sigma'_M)$ in Eq. (3) is the effective stress in the matrix. A power law expression is chosen for the function $\Phi_M(F) = F^p$ as it adequately represents the behavior of many metals [28]. A linear hardening law is chosen for the evolution of the yield strength σ_0 . The rate of evolution of σ_0 depends on the matrix equivalent plastic strain rate $\dot{\epsilon}_M^p (= \sqrt{\frac{2}{3}} \dot{\epsilon}_M^p : \dot{\epsilon}_M^p)$ and the inelastic work as:

$$\dot{\sigma}_0 = h(W_p) \dot{\epsilon}_M^p \quad (6)$$

where $h(W_p)$ is the instantaneous plastic modulus. From Eq. (4), the equivalent plastic strain rate $\dot{\epsilon}_M^p$ can be expressed in terms of the over-stress function as:

$$\dot{\epsilon}_M^p = \sqrt{\frac{2}{3}} \gamma \langle \Phi_M(F) \rangle \quad (7)$$

Returning to the rate and pressure-dependent plasticity equations governing the porous matrix material behavior, the overall plastic strain rate is derived from the associated flow rule as:

$$\dot{\epsilon}^p = \dot{\lambda} \frac{\partial \Phi^{vp}}{\partial \sigma} \quad (8)$$

where $\dot{\lambda}$ is a viscoplastic multiplier that can be derived in terms of the matrix plastic strain rate $\dot{\epsilon}_M^p$. Assuming that the Hill–Mandel micro–macro energy condition [19] governs homogenization conditions for the porous matrix material, the rate of dissipative energy in the porous matrix material can be expressed as the product of the local equivalent stress $\bar{\sigma}_M$ and equivalent strain rate $\dot{\epsilon}_M^p$ i.e.

$$\sigma : \dot{\epsilon}^p = \overline{\sigma_M : \dot{\epsilon}_M^p} = (1-f) \bar{\sigma}_M \dot{\epsilon}_M^p \quad (9)$$

The overbar in Eq. (9) corresponds to the ensemble average over a representative volume element. The viscoplastic multiplier $\dot{\lambda}$ may be obtained by substituting the flow rule (8) into the energy Eq. (9) as:

$$\dot{\lambda} = (1-f) \sqrt{\frac{2}{3}} \frac{\bar{\sigma}_M}{\sigma : \frac{\partial \Phi^{vp}}{\partial \sigma}} \gamma \langle \Phi_M(F) \rangle \quad (10)$$

The resulting flow rule is stated as:

$$\dot{\epsilon}^p = (1-f) \sqrt{\frac{2}{3}} \frac{\bar{\sigma}_M}{\sigma : \frac{\partial \Phi^{vp}}{\partial \sigma}} \gamma \langle \Phi_M(F) \rangle \frac{\partial \Phi^{vp}}{\partial \sigma} \quad (11)$$

The rate of evolution of the local macroscopic void volume fraction f is divided into growth and nucleation parts [4,35], as:

$$\dot{f} = \dot{f}_{growth} + \dot{f}_{nucleation} \quad (12)$$

The matrix void growth rate due to the dilatation is:

$$\dot{f}_{growth} = (1-f) \dot{\epsilon}_{kk}^p \quad (13)$$

The rate of plastic strain controlled void nucleation is expressed in terms of the effective plastic strain $\bar{\epsilon}_M^p$ in the underlying matrix [4] as:

$$\dot{f}_{nucleation} = A(\bar{\epsilon}_M^p) \dot{\epsilon}_M^p \quad (14)$$

where

$$A(\bar{\epsilon}_M^p) = \frac{f_N}{s_N \sqrt{2\pi}} \exp \left[-\frac{1}{2} \left(\frac{\bar{\epsilon}_M^p - \epsilon_N}{s_N} \right)^2 \right] \quad (15)$$

Here ϵ_N is the mean nucleation strain, s_N is its standard deviation, and f_N is the intensity of void nucleation.

In [26,20] a material length scale has been incorporated in the form of a nonlocal model to avoid mesh sensitivity. In this formulation, the nonlocal growth rate of the void volume fraction at a material point $\bar{\mathbf{x}}$ is given as:

$$\dot{f}^{non-local} = \frac{1}{W(\bar{\mathbf{x}})} \int_{\Omega_m} \dot{f}(\mathbf{x}) w(|\mathbf{x} - \bar{\mathbf{x}}|) d\Omega \quad (16)$$

where

$$W(\bar{\mathbf{x}}) = \int_{\Omega_m} w(|\mathbf{x} - \bar{\mathbf{x}}|) d\Omega \quad \text{and} \quad w(|\mathbf{x}|) = \left[\frac{1}{1 + (|\mathbf{x}|/L)^p} \right]^q \quad (17)$$

Here $p = 8$, $q = 2$ and $L > 0$ is a material characteristic length, which regularizes the localization problem. In classical homogenization theories, the size of the microstructural domain or RVE does not affect the solution. The use of a non-local evolution law for void volume fraction f in Eq. (17) introduces a length scale L to the problem and hence, the size of the microstructural region affects the solution. For the cast aluminum microstructure studied in this paper, numerical experiments determine that a value $L = 0.014$ regularizes the solution adequately. The weighting function $w(|\mathbf{x}|) = 1$ at $|\mathbf{x}| = 0$, $w(|\mathbf{x}|) = 0.25$ at $|\mathbf{x}| = L$ and $w(|\mathbf{x}|) \rightarrow 0 \forall |\mathbf{x}| > L$ with a narrow transition region. Non-locality is associated with spatial gradients of \dot{f} .

Finally, an acceleration function f^* is introduced in Eq. (3) to model the complete loss of material stress carrying capacity due to void coalescence [35] as:

$$f^* = \begin{cases} f & f \leq f_c \\ f_c + \frac{f_u - f_c}{f_f - f_c} (f - f_c) & f > f_c \end{cases} \quad (18)$$

f_c is the critical void volume fraction at which void coalescence first occurs and f_f is the value at final failure. As the void volume fraction $f \rightarrow f_f$, the acceleration function $f^* \rightarrow f_u^* = 1/q_1$. At this value, the yield surface shrinks to a point manifesting loss of material load capacity. To avoid numerical difficulties, $f \rightarrow 0.95f_f$ is used in Eq. (18). The value of f is frozen once it reaches $0.95f_f$ at an element quadrature point, implying local ductile material failure.

3. A rate-dependent homogenization-based continuum plasticity-damage (HCPD) model for the heterogeneous porous material

Micromechanical analyses of the heterogeneous microstructural RVEs with the constitutive models described in Section 2 are used to develop a macroscopic homogenization based continuum plasticity-damage or HCPD model for the equivalent material. The phases represented in this model are the ductile matrix containing microvoids and the brittle inclusions. The HCPD model assumes an anisotropic rate-dependent elasto-viscoplasticity framework for materials with evolving porosity. It is an extension of the equivalent viscoplastic model for non-porous materials that has been developed in [25]. In the HCPD constitutive model, the total homogenized strain rate is assumed to admit an additive decomposition into homogenized elastic and viscoplastic parts as:

$$\dot{\mathbf{e}} = \dot{\mathbf{e}}^e + \dot{\mathbf{e}}^p \quad (19)$$

For small elastic strains, the rate of homogenized Cauchy stress $\dot{\Sigma}$ is related to the elastic part of the strain rate tensor as:

$$\dot{\Sigma} = \bar{\mathbf{C}}^e : \dot{\mathbf{e}}^e \quad (20)$$

where $\bar{\mathbf{C}}^e$ is the homogenized fourth order anisotropic elasticity tensor.

Following the structure of GTN models in [16,34,35,9], the effective GTN yield function in the HCPD model is expressed as:

$$\bar{\phi} = \frac{\Sigma_{eq}^2}{(\bar{\sigma}_c)^2} + 2Q_1 \bar{f}^* \cosh \left(\frac{3Q_2}{2} \frac{\Sigma^{hyd}}{\bar{\sigma}_c} \right) - 1 - (Q_1 \bar{f}^*)^2 = 0 \quad (21)$$

$\bar{\phi}$ corresponds to the loading surface for the homogenized three phase material in the stress space. $\Sigma^{hyd} (= \frac{\Sigma_1 + \Sigma_2 + \Sigma_3}{3})$ is the homogenized hydrostatic stresses, while The homogenized equivalent stress Σ_{eq} under plane strain or plane stress conditions is expressed in the form of the anisotropic yield function in [18] as:

$$\Sigma_{eq}^2 = \hat{F}(\Sigma_{22} - \Sigma_{33})^2 + \hat{G}(\Sigma_{33} - \Sigma_{11})^2 + \hat{H}(\Sigma_{11} - \Sigma_{22})^2 + \hat{C}\Sigma_{12}^2 \quad (22)$$

Stress components are expressed in a material-damage principal coordinate system, defined in Section 3.1. The anisotropy coefficients \hat{F} , \hat{G} , \hat{H} and \hat{C} in Eq. (22) are functions of the plastic work W_p [25]. The functional forms of these coefficients in terms of W_p are determined from homogenized response of the statistically equivalent RVE or SERVE. The denominator $\bar{\sigma}_c$ is the flow stress for the rate-dependent composite material consisting of the matrix and inclusions, but without voids. Correspondingly the over-stress function \bar{F} in the viscoplasticity flow rule of [28] is expressed as:

$$\bar{F} = \bar{\sigma}_c - Y_f(W_p) \quad (23)$$

The over-stress function \bar{F} is a measure of the excess stress over the rate-independent homogenized yield strength $Y_f(W_p)$ of the heterogeneous material without any voids. Its dependence on inelastic work W_p incorporates the effect of work-hardening. \bar{f}^* is the acceleration function of the macroscopic void volume fraction \bar{f} similar to that given in (18). Finally, the parameters Q_1 and Q_2 govern the void evolution in the macroscopic model and are also determined by homogenization.

The viscoplastic strain-rate tensor is orthogonal to the loading surface in the stress space and is written as:

$$\dot{\mathbf{e}}^p = \dot{\lambda} \mathbf{N}, \quad \text{where } \mathbf{N} = \frac{\partial \bar{\phi}}{\partial \boldsymbol{\Sigma}} \quad (24)$$

The homogenized viscoplastic multiplier $\dot{\lambda}$ is obtained from the Hill–Mandel energy equivalence condition [19] governing homogenization. The rate of plastic work for the porous matrix material containing inclusions is expressed as:

$$\boldsymbol{\Sigma} : \dot{\mathbf{e}}^p = (1-f) \bar{\sigma}_c \dot{\bar{\epsilon}}_c^p = (1-f) \boldsymbol{\sigma}_c : \dot{\boldsymbol{\epsilon}}_c^p \quad (25)$$

where $\dot{\bar{\epsilon}}_c^p$ is the effective plastic strain rate in the matrix with inclusions in the absence of voids. $\boldsymbol{\sigma}_c$ and $\dot{\boldsymbol{\epsilon}}_c^p (= \dot{\lambda} \frac{\partial \bar{\phi}}{\partial \boldsymbol{\sigma}_c})$ are the stress and strain rate tensors in the underlying heterogeneous matrix material without voids. The corresponding viscoplastic multiplier according to [28] is given as:

$$\dot{\lambda} = \Gamma_0 \Phi(\bar{F}) \quad (26)$$

Γ_0 is the temperature dependent viscosity coefficient and the function is expressed in a power law form as $\Phi(\bar{F}) = \langle \bar{F} \rangle^p$. The constitutive relations have been described in [25], where the effective plastic strain rate in the matrix with inclusions is derived as $\dot{\bar{\epsilon}}^p = \dot{\lambda}$. From equations (24) and (25), the macroscopic viscoplastic multiplier for the porous heterogeneous material is obtained as:

$$\dot{\lambda} = \frac{(1-f) \bar{\sigma}_c}{\boldsymbol{\Sigma} : \mathbf{N}} \Gamma_0 \langle \bar{F} \rangle^p \quad (27)$$

Finally, the rates of plastic work and void volume fraction are defined as:

$$\dot{W}_p = \boldsymbol{\Sigma} : \dot{\mathbf{e}}^p \quad (28)$$

$$\dot{f} = \dot{f}_{\text{growth}} + \dot{f}_{\text{nucleation}} \quad (29)$$

The homogenized void growth law is the same as in (13) [9], i.e. $\dot{f}_{\text{growth}} = (1-f) \dot{\epsilon}_{kk}^p$. This results from plastic incompressibility of the underlying matrix without voids. The void nucleation law $\dot{f}_{\text{nucleation}}$ is however a novel contribution of this work that will be discussed later in Section 3.2.

3.1. Evolving anisotropy

The set of Eqs. (19)–(24) and (27)–(29) forms the constitutive model for the rate-dependent macroscopic simulation of porous ductile material with inclusions, i.e. the rate-dependent HCPD model. It is important that this constitutive model be described in an evolving material principal coordinate system. This system takes into account the effects of deformation and damage histories on the evolution of anisotropy. As discussed in [9,25], initial macroscopic material anisotropy is due to the presence of heterogeneities, e.g. brittle inclusions, in the microstructure. However, this anisotropy evolves with deformation and void growth due to nonuniform and constrained plastic flow in the micro-channels between heterogeneities. The equivalent stress Σ_{eq} in Eq. (21) is designed to accommodate both initial and evolving anisotropy. For plane strain problems, it is expressed using the anisotropic yield function Eq. (22).

The stress components, as well as other tensor variables, in the constitutive model are represented in the principal axes of material anisotropy that evolves with deformation. The material is assumed to remain orthotropic in this system throughout the deformation process. The use of this material coordinate system has been shown in [9] to capture the effects of non-proportional load and deformation histories with very good accuracy. The angle β , delineating the principal axes of anisotropy for plane strain analysis, is determined in every increment from the condition that the transformed tangent modulus (E_{ijkl}^{tan}) in this system remains orthotropic. This condition renders the terms coupling normal and shear components of the tangent modulus to be equal to zero, i.e.

$$(E_{1112}^{\text{tan}})' = (E_{2212}^{\text{tan}})' = (E_{3312}^{\text{tan}})' = 0, \quad (30)$$

where $(E_{ijkl}^{\text{tan}})' = Q_{im} Q_{jn} Q_{kp} Q_{lq} E_{mnpq}^{\text{tan}}$. The rotation matrix is expressed as:

$$[\mathbf{Q}] = \begin{bmatrix} \cos \beta & \sin \beta & 0 \\ -\sin \beta & \cos \beta & 0 \\ 0 & 0 & 1 \end{bmatrix}$$

Anisotropy parameters \hat{F} , \hat{G} , \hat{H} and \hat{C} in Eq. (22) are calibrated with respect to this principal coordinate system from homogenization. These parameters evolve due to the constrained plastic flow resulting from the presence of heterogeneities.

3.2. Rate-dependent void nucleation criterion

Ductile failure in many metallic alloys such as cast aluminum initiates with inclusion fragmentation, which results in void nucleation and growth. This microscopic damage mechanism manifests in the macroscopic rate-dependent HCPD model as void nucleation in the microstructure. The void nucleation model proposed in this paper is an extension of the strain based

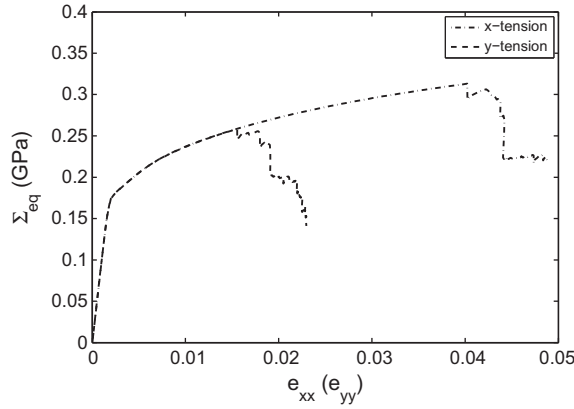


Fig. 2. Comparison of macroscopic stress–strain response of RVE 1 in Fig. 5a for two mutually perpendicular loading directions in tension.

rate-independent nucleation law in [9]. The morphology and distribution of inclusions is highly significant in governing damage evolution in a porous ductile material with heterogeneities [37,26]. The rate-independent macroscopic damage response of an RVE is plotted for two different tension loading directions in Fig. 2. It shows that the damage evolution process is highly anisotropic.

In addition to morphological characteristics, the rate of deformation also plays a significant role on the microstructural damage evolution. Sensitivity studies of ductile failure for different loading rates in [26,27] have concluded that the applied strain-rate plays an important role on ductile fracture. The inclusion stresses are much higher for higher strain-rates than for lower strain rates. This causes inclusion cracking at significantly lower strains. In addition, the matrix phase undergoes lower plastic deformation at higher strain rates. This reduces void growth and localization of damage near cracked inclusions. Strain to failure in heterogeneous ductile materials is thus governed by the competition between these two effects. The void nucleation model in this paper is designed to accommodate this pronounced anisotropy and rate dependence of inclusion cracking.

The homogenized void nucleation criterion in the HCPD model follows that for the inclusion cracking model discussed in Section 2. However, instead of dependence on the local stresses as in Eq. (1), the homogenized nucleation criterion is expressed in terms of the macroscopic strains [9]. The HCPD void nucleation model follows the Weibull statistics based probability of fracture \bar{P}_{fr} , and is expressed in terms of local strains and inclusion size v as:

$$\bar{P}_{fr}(v, \hat{e}, \dot{\hat{e}}) = 1 - \exp \left[-\frac{v}{v_0} \left(\frac{\hat{e}}{e_0(\dot{\hat{e}})} \right)^{m(\dot{\hat{e}})} \right] \tag{31}$$

Here e_0 and m are the Weibull parameters that are functions of local strain rate $\dot{\hat{e}}$, and \hat{e} is an effective strain measure expressed as:

$$\hat{e} = \langle A(\theta_p)\bar{e}_1 + B(\theta_p)\bar{e}_2 + C(\theta_p)\bar{e}_3 \rangle \tag{32}$$

Here \bar{e}_1 , \bar{e}_2 and \bar{e}_3 are macroscopic principal strains and $\langle \ \rangle$ is the MacCauley operator. Coefficients A , B and C are functions of the angle of principal strain θ_p . Their functional forms are calibrated from micromechanical LE-VCFEM analysis of the RVE. This dependence provides an effective way of incorporating damage anisotropy emerging from morphology and distribution of inclusions in the microstructure.

The area fraction of cracked inclusions for an applied constant strain-rate $\dot{\hat{e}}$ is denoted by $\rho_c(\hat{e}, \dot{\hat{e}})$. It is expressed in terms of the probability density function of the inclusion size $p(v)$ and the probability of fracture $\bar{P}_{fr}(v, \hat{e}, \dot{\hat{e}})$ as:

$$\rho_c(\hat{e}, \dot{\hat{e}}) = \int_0^\infty \frac{v}{v_0} p(v) \bar{P}_{fr}(v, \hat{e}, \dot{\hat{e}}) dv \tag{33}$$

where $p(v)$ is the probability of finding an inclusion of size v . For a discrete distribution of inclusions in a finite sized RVE, the probability density function $p(v)$ is written as the discrete sum:

$$p(v) = \sum_{i=1}^N \delta(v - v_i) p(v_i) \tag{34}$$

where $\delta(\)$ is the Dirac delta function. N is the number of discrete divisions V_i in the range of volume fractions in the probability density function $p(v)$. Substituting Eq. (34) into Eq. (33), yields:

$$\rho_c(\hat{e}, \dot{\hat{e}}) = \int_0^\infty \frac{v}{v_0} \left[\sum_{i=1}^N \delta(v - v_i) p(v_i) \right] \bar{P}_{fr}(v, \hat{e}, \dot{\hat{e}}) dv = \sum_{i=1}^N \int_0^\infty \frac{v}{v_0} [\delta(v - v_i) p(v_i)] \bar{P}_{fr}(v, \hat{e}, \dot{\hat{e}}) dv \tag{35}$$

This leads to the following expression for the area fraction of cracked inclusions:

$$\rho_c(\hat{e}, \dot{\hat{e}}) = \sum_{i=1}^N \frac{v_i}{v_0} p(v_i) \bar{P}_{fr}(v_i, \hat{e}, \dot{\hat{e}}) = \sum_{i=1}^N \frac{v_i}{v_0} p(v_i) \left(1 - \exp \left[-\frac{v_i}{v_0} \left(\frac{\hat{e}}{e_0(\dot{\hat{e}})} \right)^{m(\dot{\hat{e}})} \right] \right) \quad (36)$$

If all the particles have the same size, i.e. $N = 1, p(v_1) = 1$, the area fraction of cracked inclusion can be derived from Eq. (36) as:

$$\rho_c(\hat{e}, \dot{\hat{e}}) = 1 - \exp \left[-\left(\frac{\hat{e}}{e_0(\dot{\hat{e}})} \right)^{m(\dot{\hat{e}})} \right] \quad (37)$$

Eqs. (36) and (37) yield the area fractions ρ_c of cracked inclusions for a fixed strain-rate throughout the load history. The parameters e_0 and m in Eq. (31) however, vary with the local strain-rate. To accommodate the effect of variation in local strain-rates, the rate of evolution of the area fraction of cracked inclusions ρ , is assumed to be governed by the relation:

$$\dot{\rho} = \tilde{k}^* \frac{d\rho_c(\hat{e}, \dot{\hat{e}})}{d\hat{e}} \dot{\hat{e}} \quad (38)$$

The factor \tilde{k}^* is introduced to account for the instantaneous change in strain rates. It reflects two scenarios corresponding to the increase or decrease of the local strain rate at a material point. For an increase in the local strain rate, the instantaneous fraction of cracked inclusions $\rho(\hat{e})$ is less than the instantaneous fraction of cracked inclusions at a constant strain rate $\rho_c(\hat{e}, \dot{\hat{e}})$. This is clearly shown in Fig. 3. The inclusion stress increase resulting from the strain rate increase will cause additional inclusion cracking in comparison with that for the constant higher strain rate loading. This increase in inclusion cracking is quantified by the factor $\tilde{k}^* = \frac{1-\rho}{1-\rho_c(\hat{e}, \dot{\hat{e}})} > 1$ in Eq. (38), which ensures that $\lim_{\hat{e} \rightarrow \infty} \rho(\hat{e}) = 1$.

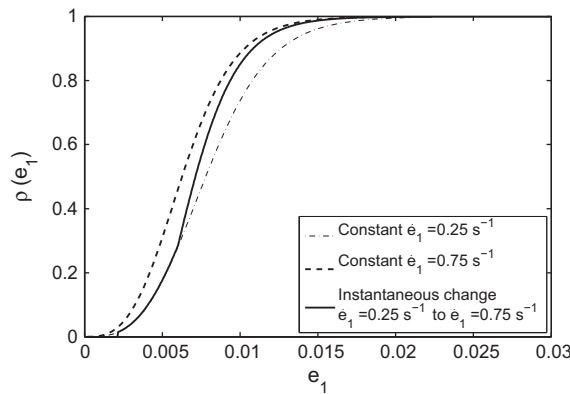


Fig. 3. Area fraction of cracked inclusions ρ within RVE 1 in Fig. 5a as a function of the principal strain e_1 for an instantaneous change in loading strain rate from 0.75 s^{-1} to 0.25 s^{-1} . The only nonzero strain component is \bar{e}_1 .

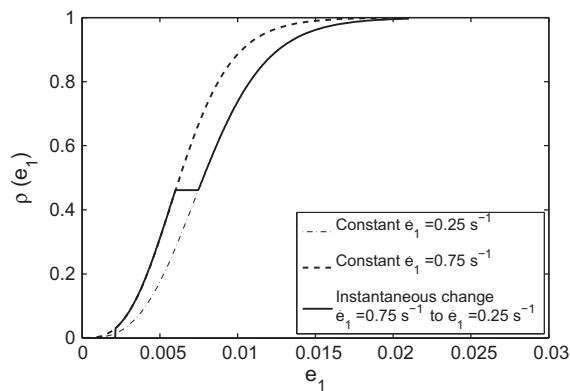


Fig. 4. Area fraction of cracked inclusions ρ within RVE 1 in Fig. 5a as a function of the principal strain \bar{e}_1 for an instantaneous change in loading strain rate from 0.25 s^{-1} to 0.75 s^{-1} . The only nonzero strain component is \bar{e}_1 .

When there is a decrease in local strain rate, the instantaneous fraction of cracked inclusions $\rho(\dot{\epsilon})$ exceeds the instantaneous fraction of cracked inclusions at a constant strain rate $\rho_c(\dot{\epsilon}, \dot{\epsilon})$, as shown in Fig. 4. This causes a stress reduction in the inclusions due to decreased strain rate. Consequently, there is a temporary arrest of inclusion cracking as long as $\rho(\dot{\epsilon}) > \rho_c(\dot{\epsilon}, \dot{\epsilon})$. This is quantified by the factor $\tilde{k}^* = 0$ in Eq. (38). In summary, the nucleation factor is expressed as

$$\tilde{k}^* = \begin{cases} \tilde{k} & \text{if } \tilde{k} \geq 1 \\ 0 & \text{if } \tilde{k} < 1 \end{cases} \quad \text{where } \tilde{k} = \frac{1 - \rho}{1 - \rho_c(\dot{\epsilon}, \dot{\epsilon})} \quad (39)$$

The void nucleation rate model in the rate-dependent HCPD model may then be expressed in the form:

$$\dot{f}_{\text{nucleation}} = V_p \dot{\rho} \quad (40)$$

V_p is a material parameter that is calibrated from micro-mechanically simulated volume fractions of cracked inclusions at given strain. The complete calibration procedure for the parameters e_0 , m , V_p , A , B and C is detailed in Section 4.3.

3.3. Numerical implementation of the rate-dependent HCPD model

The numerical implementation of the macroscopic rate-dependent HCPD model includes the return mapping algorithm for rate-dependent plasticity developed in [1]. This algorithm consists of an initial elastic predictor step, where the elastic response is assumed and the stresses are predicted. This is followed by the plastic corrector step which returns the stress to the updated loading surface in stress space determined by the viscoplastic flow rule. The numerical stress update algorithm is incorporated in the commercial code *MSC-Nastran Marc* through the user interface subroutine *Uvscpl()*.

4. Calibration of material parameters in the rate-dependent HCPD model

The rate-dependent HCPD model parameters are calibrated from homogenized quantities obtained from asymptotic expansion homogenization (AEH) of micromechanical variables from LE-VCFEM simulations. These homogenized quantities include the macroscopic strain $\bar{\epsilon}$, plastic strain \bar{e}^p , stress Σ and plastic work W_p . The parameters are calibrated in the material principal coordinate system following the procedure outlined for rate-independent materials with damage in [9] and for rate-dependent materials without damage in [25].

Calibration of microstructure dependent parameters is performed for three different microstructural RVE's. Two computer generated RVE's, denoted by RVE 1 and RVE 2, are shown in Fig. 5. The third RVE, denoted by RVE 3, is shown in Fig. 1b and obtained from a micrograph of an actual microstructure of a cast aluminum alloy W319. The LE-VCFEM micromechanics model used for the RVE's simulations is described in [8,26] and will not be repeated in this paper for sake of brevity. The sets of LE-VCFEM parameters used for these simulations are reported in Tables 1 and 2. The plastic hardening curve of the aluminum matrix without voids and particles used for the LE-VCFEM simulations is given in Fig. 6.

4.1. Plasticity parameters in the HCPD model

The plasticity material parameters of the rate-dependent HCPD model include $\hat{F}(W_p)$, $\hat{G}(W_p)$, $\hat{H}(W_p)$ (normalized with respect to $\hat{C}(W_p)$) in Eq. (22), $Y_f(W_p)$ in Eq. (23), and Γ_0 and P in Eq. (27). They are calibrated from the homogenized values of state variables from micromechanics LE-VCFEM simulations. All of the parameters are calibrated in the material principal coordinate system following the procedure described in [9,25]. Prior to the calibration of the plasticity parameters, the fourth

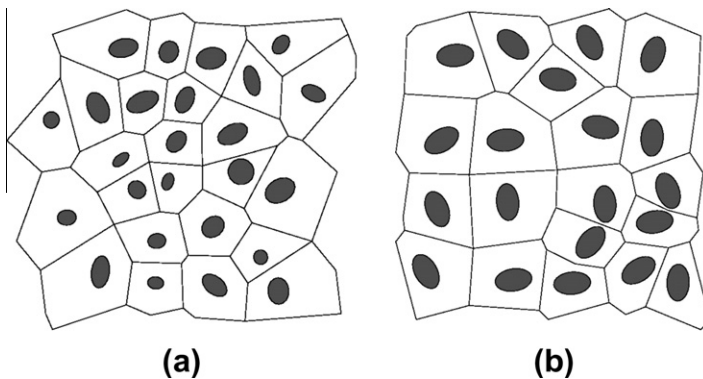


Fig. 5. Computer generated microstructures with the following characteristics: (a) RVE 1: inclusion volume fraction 10% with 25 elliptical inclusions of random shape and orientation in a hardcore dispersion (48 μm \times 48 μm), (b) RVE 2: inclusion volume fraction 15% with 20 identical elliptical inclusions in a hardcore dispersion (48 μm \times 48 μm).

Table 1
Elastic and cracking properties of inclusion in LE-VCFEM [26].

RVE	E (GPa)	ν	σ_w (MPa)	m	v_0	P_{frag}^{cr} (%)
1	320	0.25	500	2.4	0.0040	97
2	320	0.25	500	2.4	0.0075	97
3	165	0.27	680	2.4	0.0036	55

Table 2
Elastic, plastic and void evolution properties of aluminum matrix in LE-VCFEM [26].

RVE	E (GPa)	ν	γ_0 (GPa ⁻¹ s ⁻¹)	p	f_0	f_c	f_f
1 & 2	72	0.22	8.086	1	0.01	0.15	0.25
3	70	0.35	8.086	1	0.01	0.15	0.25

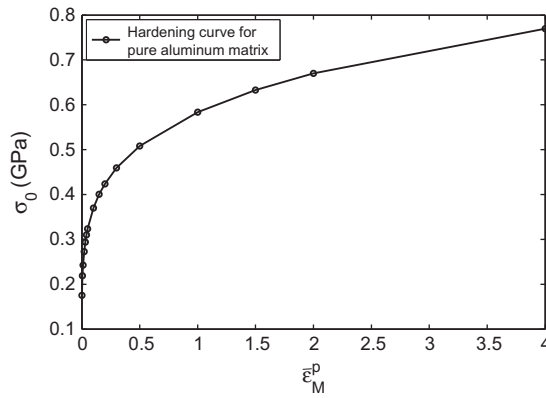


Fig. 6. Stress–strain (hardening) curve for the aluminum matrix used for the micromechanics LE-VCFEM simulations.

order anisotropy elasticity tensor $\bar{\mathbf{C}}^e$ is computed numerically by applying four independent macroscopic strains on an unloaded RVE and obtaining the resulting homogenized stress tensors. The strain increment $\bar{e}_{zz} = \epsilon$ is applied using the generalized plane strain constraint conditions [20,26]. The macroscopic yield strength $Y_f(W_p)$ and the anisotropy parameters $\hat{F}(W_p)$, $\hat{G}(W_p)$ and $\hat{H}(W_p)$ are calibrated from the homogenized responses of rate-independent LE-VCFEM simulations of the RVE. The anisotropy parameters and yield strength are shown in Fig. 7. The viscoplastic material parameters Γ_0 and P are calibrated following the procedure described in [25]. The homogenized viscoplastic parameters calibrated for the RVE's 1, 2 and 3 are given in Table 3.

4.2. Damage parameters Q_1 and Q_2

Parameters Q_1 and Q_2 in Eq. (21), which govern the void evolution in the macroscopic rate-dependent HCPD model, are calibrated from a set of LE-VCFEM micromechanical simulations of the RVE containing porous metallic matrix with inclusions. Homogenization is performed on these micromechanical simulations and the calibration proceeds in the following steps:

- (1) A rate-independent LE-VCFEM simulation of the RVE is conducted with the applied macroscopic shear strain components $\bar{e}_{xx} = 0$; $\bar{e}_{yy} = 0$; $\bar{e}_{xy} \neq 0$. The initial averaged void volume fraction of the RVE is f_0 . The corresponding macroscopic stress tensor $\bar{\Sigma}$ and averaged void volume fraction f are evaluated and plotted as functions of the macroscopic plastic work W_p . Since the normal stresses $\Sigma_{xx} = \Sigma_{yy} = \Sigma_{zz} = 0$ for this loading conditions, and also the hydrostatic part of plastic strain $\bar{e}_{kk}^p = 0$, the void volume fraction does not change, i.e. $f = f_0$. The parameter Q_1 can be solved from Eq. (21) as:

$$Q_1 = \frac{1}{f_0} \left(1 - \frac{\sqrt{3}\bar{\Sigma}_{xy}}{Y_f} \right) \quad (41)$$

- (2) For calibrating Q_2 , micromechanical LE-VCFEM simulations are conducted for N different loading conditions with non-zero, evolving void volume fraction. Loading conditions are prescribed with different macroscopic strain ratios

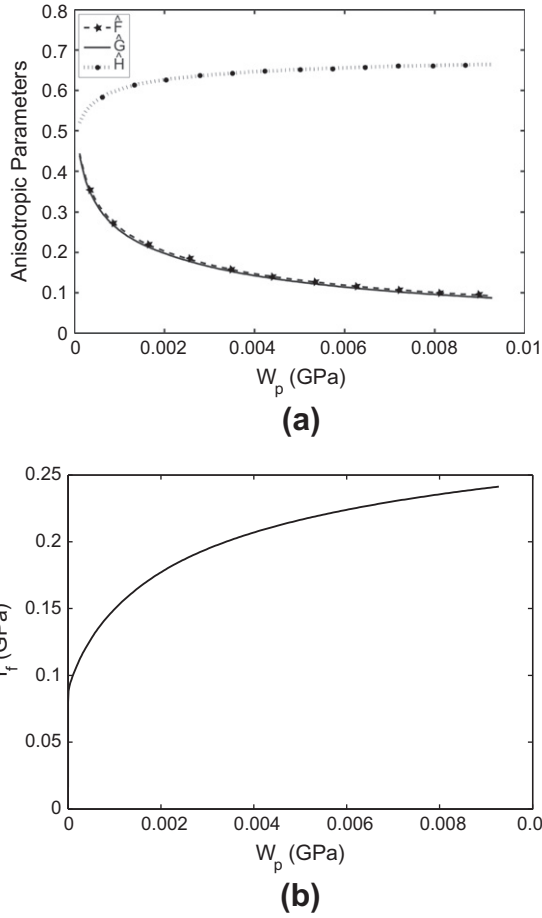


Fig. 7. (a) Evolution of anisotropy parameters \hat{F} , \hat{G} and \hat{H} with plastic work for RVE 1 in Fig. 5(a), (b) yield stress in shear Y_f with plastic work for RVE 1 in Fig. 5a.

Table 3
Homogenized viscoplastic material parameters Γ_0 and P .

RVE	Γ_0 (GPa ⁻¹ s ⁻¹)	P
1	4.83	1
2	4.72	1
3	6.13	1

$\bar{e}_{xx} : \bar{e}_{yy} : \bar{e}_{xy}$. At the end of each strain increment homogenization is conducted and the tangent stiffness E_{ijkl}^{tan} is evaluated. Subsequently the material principal coordinate system is determined from Eq. (30). For a given value of plastic work W_p , the parameter Q_2 is evaluated from known values of \hat{F} , \hat{G} , \hat{H} , Y_f and Q_1 by solving the minimization problem:

$$\min_{Q_2} \sum_{i=1}^N \left[\frac{\Sigma_{eq}^2}{Y_f^2} + 2Q_1 f \cosh \left(\frac{3Q_2 \Sigma^{hyd}}{2 Y_f} \right) - 1 - (Q_1 f)^2 \right]^2 \quad (42)$$

It has been demonstrated in [9] that the calibrated values of Q_1 and Q_2 for the different RVE's exhibit only minimal dependence on plastic work. The calculated mean and standard deviation of Q_1 and Q_2 for the three RVE's are listed in Table 4. The standard deviations of Q_1 and Q_2 are very small compared to the mean values and hence Q_1 and Q_2 for each RVE are taken as constants in the analyses, as concluded in [9]. The parameters Q_1 and Q_2 depend on the microstructure they are calibrated for. The Q_1 values are quite different from the value in the pure matrix material ($q_1 = 1.5$). This variation is attributed mainly to presence of inclusions with a volume fraction V_f .

Table 4Mean and standard deviation of the calibrated parameters Q_1 and Q_2 for different RVE's.

	Mean of Q_1	Standard dev. of Q_1	Mean of Q_2	Standard dev. of Q_2
RVE 1	1.70	0.0065	1.04	0.0179
RVE 2	1.77	0.0026	1.09	0.0064
RVE 3	1.89	0.0103	1.01	0.0087

4.3. Calibration of parameters in the void nucleation model

Calibration of parameters in the rate-dependent void nucleation criterion is executed in two steps. The first step involves the calibration of local strain-rate dependent parameters e_0 and m in Eqs. (36) and (37). The second step involves the calibration of anisotropy parameters $A(\theta_p)$, $B(\theta_p)$ and $C(\theta_p)$ in Eq. (32) that are functions of the angle of principal strain θ_p . Rate-dependent LE-VCFEM simulations with void evolution and inclusion cracking, along with rate-dependent HCPD model analyses are conducted for calibrating the required parameters.

4.3.1. Parameters e_0 and m

The parameters e_0 and m in Eqs. (36) and (37), defining the area fraction of cracked particles at constant strain rate $\rho_c(\dot{\epsilon}, \dot{\epsilon})$ are functions of the local strain rate. These two parameters govern the rate-dependency of damage evolution. In order to calibrate e_0 and m , a total of K micromechanical LE-VCFEM simulations with constant strain-rates spread evenly in the required range are performed for the macroscopic HCPD model. All the micromechanical simulations are performed under applied macroscopic strain conditions $\bar{e}_{xx} \neq 0$; $\bar{e}_{yy} = 0$; $\bar{e}_{xy} = 0$. Thus \hat{e} in Eq. (32) reduces to $\hat{e} = A\bar{e}_1 = \bar{e}_1$ by setting the parameter $A(\theta_p = 0^\circ) = 1$. For each of the K micromechanical simulations, e_0 and m are calculated, so that a best fit is obtained between the Eq. (36) or (37) and micromechanics results for the area fraction of cracked particles. Once the calibration is completed for all the K applied strain rates, the parameters e_0 and m can be expressed as functions of the local strain rate $\dot{\epsilon}$.

The two parameters are calibrated for RVE 1 shown in Fig. 5a. A total of $K = 10$ LE-VCFEM simulations with applied strain-rates in the range 0.01 – 0.75 s^{-1} are performed. Fig. 8 shows the micromechanics result for the area fraction of cracked particles at an applied strain rate of 0.1 s^{-1} as a function of the principal strain e_1 along with the fitted curve of Eq. (37) for the values $e_0 = 0.009739$ and $m = 3.11$. Figs. 9 and 10 show the discrete calibrated values and the corresponding functional fit for the parameters e_0 and m calibrated for RVE 1. It is observed in Figs. 9 and 10 that there are two distinct mechanisms taking place due to rate-dependency. At lower strain rates with inclusion cracking, voids start to nucleate near the tip of the cracked inclusions and subsequently coalesce to cause matrix failure in the microstructure. This results in damage localization and failure of the material. On the other hand, at higher strain rates, the matrix response is mainly elastic. Therefore void nucleation in the matrix and growth is reduced and no damage localization occurs in the microstructure. This results in different behavior of the e_0 and m curves in the Figs. 9 and 10 for higher and lower strain rates.

4.3.2. Calibration of parameters A , B and C

In order to calibrate the anisotropy parameters $A(\theta_p)$, $B(\theta_p)$ and $C(\theta_p)$ in Eq. (32), a total of four LE-VCFEM simulations at a strain-rate in the given range, used in Section 4.3.1, are executed. The four simulations with different loading conditions are:

- (1) Tension in y-direction with constrained transverse strain components ($e_{xx} = 0$; $e_{yy} \neq 0$; $e_{xy} = 0$).
- (2) Biaxial tension ($e_{xx} = e_{yy} \neq 0$; $e_{xy} = 0$).
- (3) One simulation with strain ratios ($e_{xx} > 0$; $e_{yy} < 0$; $e_{xy} = 0$).
- (4) One simulation with strain ratios ($e_{xx} < 0$; $e_{yy} > 0$; $e_{xy} = 0$).

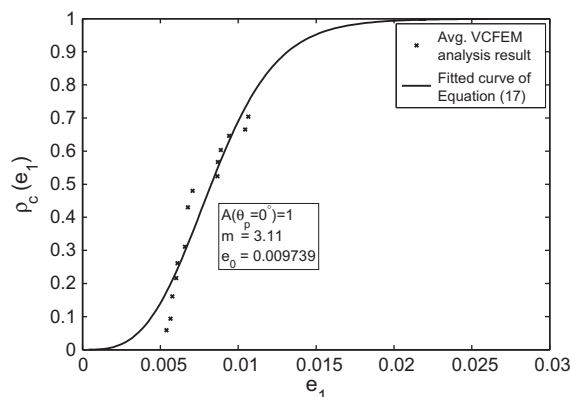


Fig. 8. Area fraction of cracked inclusions from LE-VCFEM analysis of RVE 1 shown in Fig. 5a at an applied strain rate of 0.1 s^{-1} , along with the best fit of Eq. (36).

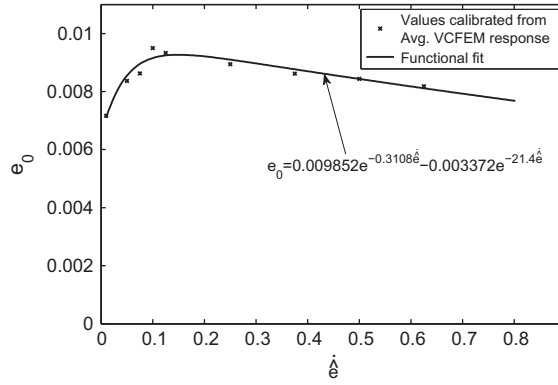


Fig. 9. Evolution of parameter e_0 with local strain rate $\dot{\epsilon}$ for RVE 1 in Fig. 5a from LE-VCFEM results along with the functional fit.

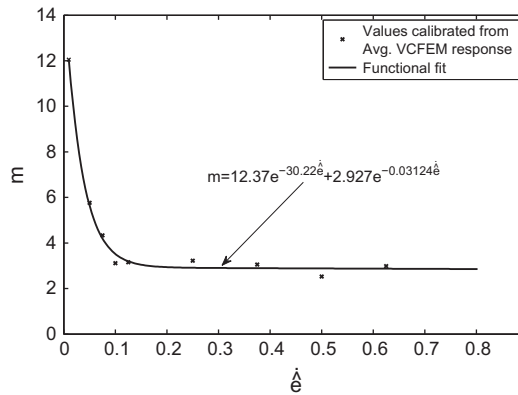


Fig. 10. Evolution of parameter m with the local strain rate $\dot{\epsilon}$ for RVE 1 in Fig. 5a from LE-VCFEM results along with the functional fit.

The anisotropy parameters A , B and C , expressed in terms of the principal strain angle θ_p , have functional forms of an ellipse in a polar plot. The angle corresponds to the principal strain angle θ_p and the radius is the value of the parameter. In Section 4.3.1, the radius of the ellipse describing the parameter A at $\theta_p = 0^\circ$ is set to 1. This value $A(\theta_p = 0^\circ) = 1$ is one of the axes of the ellipse describing A . The other axis of the ellipse is obtained from the y -direction tension with constrained transverse strain loading (1). The value of A at $\theta_p = 90^\circ$ is evaluated by fitting either Eq. (36) or (37) with the micromechanics results. The values of e_0 and m at the effective strain rate $\dot{\epsilon}$ are obtained from the functional forms calibrated in Section 4.3.1. For RVE 1 of Fig. 5a, the area fraction of fractured inclusion ρ is plotted as a function of the principal strain $\bar{\epsilon}_1$ in Fig. 11 for this loading condition. Fig. 12 shows the functional form of parameter $A(\theta_p)$.

Similar to A , the major and minor axes of the ellipse describing the parameter B can be obtained from the biaxial tension loading test (2). Since for the biaxial tension test, the angle of principal strain $\theta_p = 0^\circ$ or 90° , only one of the axes of the ellipse needs to be determined. If the angle of principal strain is taken as $\theta_p = 0^\circ$, then $A(\theta_p) = 1$ and the effective strain is $\hat{\epsilon} = A\bar{\epsilon}_1 + B\bar{\epsilon}_2$. Once again, either Eq. (36) or (37) is fitted with the micromechanics result for the area fraction of cracked particles needed to evaluate the value of B at $\theta_p = 0^\circ$. The other axis of the B -ellipse can be obtained as:

$$B(\theta_p = 90^\circ) = A(\theta_p = 0^\circ) + B(\theta_p = 0^\circ) - A(\theta_p = 90^\circ)$$

The other two loading conditions, viz. $(e_{xx} > 0; e_{yy} < 0; e_{xy} = 0)$ and $(e_{xx} < 0; e_{yy} > 0; e_{xy} = 0)$ are used to calibrate the major and minor axes of the elliptical form of the parameter C . The values of major and minor axes of A , B and C for RVE's 1, 2 and 3 in Figs. 5 and 1b are given in Table 5.

4.3.3. Calibration of parameter V_p

The parameter V_p in Eq. (40), which relates the rate of cracked inclusions to the rate of void nucleation in the rate-dependent HCPD model, is evaluated iteratively by minimizing the difference between the LE-VCFEM micromechanical analyses and rate-dependent HCPD macroscopic analyses, following the condition

$$\min_{V_p} \sum_{i=1}^N \sum_{j=1}^{M_i} \left\| \Sigma_{\text{HCPD}}^{ij} - \Sigma_{\text{micro}}^{ij} \right\|_F^2 \tag{43}$$

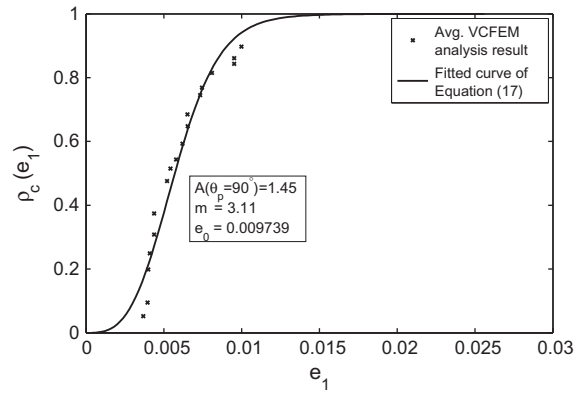


Fig. 11. Area fraction of cracked inclusions for the y -direction tension with constrained transverse strain by LE-VCFEM analysis of RVE 1 at a strain-rate of 0.1 s^{-1} , along with the fit of Eq. (36).

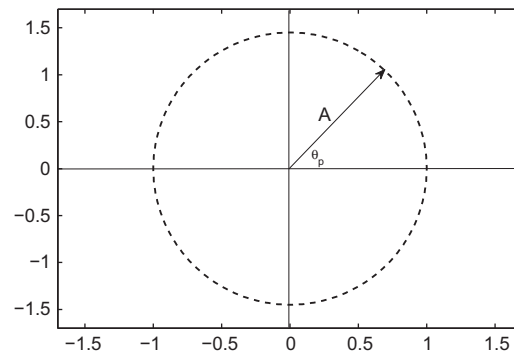


Fig. 12. Void nucleation anisotropy parameter A as a function of the angle of principal strain angle θ_p for RVE 1.

Table 5

Values of anisotropy parameters A , B and C at different principal strain angles θ_p . $A(\theta_p = 0^\circ) = 1$ for all RVE's.

	$A(\theta_p = 90^\circ)$	$B(\theta_p = 0^\circ)$	$B(\theta_p = 90^\circ)$	$C(\theta_p = 0^\circ)$	$C(\theta_p = 90^\circ)$
RVE 1	1.45	1.51	1.06	0.90	1.34
RVE 2	1.28	1.39	1.10	0.96	1.10
RVE 3	1.01	0.67	0.66	0.66	0.69

Here N is the total number of simulations performed and M_i is the number of increments in the i th micromechanical simulation. The error is measured with the Frobenius norm of the stress difference between macroscopic and microscopic simulations.

5. Validation of the rate-dependent HCPD model

The rate-dependent HCPD model is validated by comparing the results of macroscopic finite element simulations with those obtained from the homogenization of micromechanics LE-VCFEM analyses. Since the rate-dependent HCPD model is an extension of the model proposed in [9], validation presented in this section is focused on rate-dependent behavior, especially on the rate-dependent void-nucleation model. All macroscopic simulations in this section are conducted with the commercial software *MSC-Nastran Marc* code, with a single four-noded *QUAD4* element. Material properties used for the LE-VCFEM micromechanics simulations are given in Tables 1 and 2 unless otherwise stated.

5.1. Viscoplastic response and void growth model

The RVE 1 in Fig. 5a has an inclusion volume fraction $V_f = 10\%$ and is characterized by a hard core dispersion of 25 elliptical inclusions with random sizes, shapes (aspect ratios) and orientations. Micromechanical analyses of this RVE is used to val-

idate the elastic–viscoplastic response of the HCPD model. Four different LE-VCFEM simulations with imposed simple shear loading are conducted with different loading strain-rates $\dot{\bar{e}}_{xy}$ and initial void volume fractions f_0 . The rate-dependent HCPD model plasticity and void related parameters for the RVE are calibrated following the procedures described in Sections 4.1 and 4.2. The homogenized shear stress Σ_{xy} from LE-VCFEM simulations is compared with the macroscopic shear stress from the rate-dependent HCPD model in Fig. 13. An excellent agreement is found between the two simulations.

Additional numerical experiments are undertaken to validate the macroscopic model for a x -direction tension with constrained transverse strain ($\bar{e}_{xx} \neq 0; \bar{e}_{yy} = 0; \bar{e}_{xy} = 0$) and an applied strain-rate $\dot{\bar{e}}_{xx} = 0.25 \text{ s}^{-1}$. The response of the HCPD model is compared with micromechanical simulation in Fig. 14. Again, an excellent agreement can be observed between the two solutions.

5.2. Void nucleation model and changes in local strain-rate

The void nucleation model is validated by simulating RVE 1 again. Parameters e_0, m, A, B and C are calibrated following the procedure described in Section 4.3 and the functional fits of the local strain-rate dependent parameters e_0 and m are shown in Figs. 9 and 10. The major and minor axes of the ellipses describing the damage anisotropy parameters A, B and C are given in Table 5. In order to validate the rate-dependent nucleation model, four micromechanics LE-VCFEM simulations are conducted, they are:

- (1) Tension in x -direction with constrained transverse strain ($\bar{e}_{xx} \neq 0; \bar{e}_{yy} = 0; \bar{e}_{xy} = 0$) at a loading strain-rate $\dot{\bar{e}}_{xx} = 0.25 \text{ s}^{-1}$.
- (2) Tension in x -direction with constrained transverse strain ($\bar{e}_{xx} \neq 0; \bar{e}_{yy} = 0; \bar{e}_{xy} = 0$) at a loading strain-rate $\dot{\bar{e}}_{xx} = 0.75 \text{ s}^{-1}$.
- (3) Tension in x -direction with constrained transverse strain ($\bar{e}_{xx} \neq 0; \bar{e}_{yy} = 0; \bar{e}_{xy} = 0$) at an initial loading strain-rate $\dot{\bar{e}}_{xx} = 0.25 \text{ s}^{-1}$, which is increased to $\dot{\bar{e}}_{xx} = 0.75 \text{ s}^{-1}$ at an applied strain $\bar{e}_{xx} = 0.6\%$.

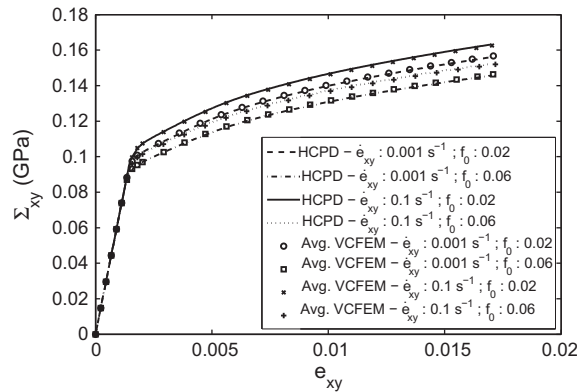


Fig. 13. Comparison of macroscopic stress–strain response in simple shear by the rate-dependent HCPD model and the micromechanical LE-VCFEM for RVE 1 in Fig. 5a. Different applied strain rates $\dot{\bar{e}}_{xy}$ and initial void volume fractions f_0 are considered.

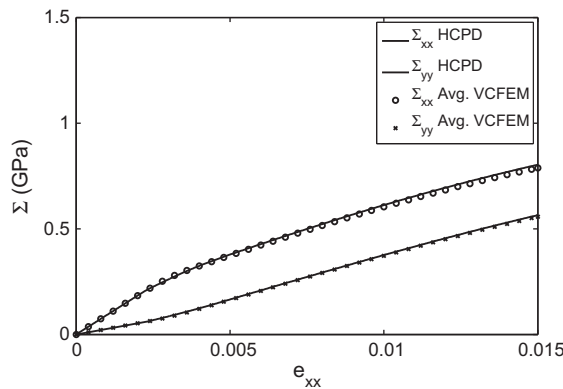


Fig. 14. Comparison of the macroscopic stress–strain responses of the rate-dependent HCPD model and the micromechanical LE-VCFEM for RVE 1 in Fig. 5a. The applied strain ratio is $\bar{e}_{xx} \neq 0; \bar{e}_{yy} = 0; \bar{e}_{xy} = 0$.

- (4) Tension in x -direction with constrained transverse strain ($\bar{e}_{xx} \neq 0; \bar{e}_{yy} = 0; \bar{e}_{xy} = 0$) at an initial loading strain-rate $\dot{\bar{e}}_{xx} = 0.75\text{s}^{-1}$, which is decreased to $\dot{\bar{e}}_{xx} = 0.25\text{s}^{-1}$ at an applied strain $\bar{e}_{xx} = 0.6\%$.

The homogenized responses of the LE-VCFEM micromechanics simulations are compared with the respective HCPD model simulation results in Figs. 15 and 16. For both HCPD and LE-VCFEM simulations, the macroscopic equivalent stress Σ_{eq} is plotted as a function of the applied strain. The micromechanics simulations show discrete drops in stress due to explicit inclusions cracking. However the HCPD model does not exhibit this behavior due to the continuous function used in the void nucleation model. A very good match is found between the HCPD and micromechanical simulation results for all the cases.

The evolution of the macroscopic area fraction of cracked inclusions ρ obtained with the rate-dependent HCPD model are plotted in Figs. 3 and 4 for loading cases (3) and (4) respectively. Loading (3) includes an instantaneous change in applied strain rate from 0.25s^{-1} to 0.75s^{-1} at an applied strain $\bar{e}_{xx} = 0.6\%$, while loading (4) includes an instantaneous change in strain rate from 0.75s^{-1} to 0.25s^{-1} . The factor k^* in Eq. (38) takes care of the instantaneous change in local strain rate, accelerating and stalling the nucleation of voids as required. The excellent matches in Figs. 15 and 16 confirm that the proposed model captures with high accuracy instantaneous changes of local strain rate.

5.3. Void nucleation model and anisotropy

The ability of the rate-dependent void nucleation model to capture material anisotropy in damage is validated by comparing with the homogenized response of different micromechanical LE-VCFEM simulations subjected to different loading conditions. Simulations are conducted for a number of applied macroscopic strain ratios ($\bar{e}_{xx} : \bar{e}_{yy} : \bar{e}_{xy}$) at an applied strain rate $\max(|\dot{\bar{e}}_{ij}|) = 0.1\text{s}^{-1}$. The respective values of the parameters A , B and C are obtained from the calibrated elliptical forms and the value of principal strain angle θ_p . The comparison between the LE-VCFEM micromechanics results and the HCPD model results in Fig. 17 show excellent agreement.

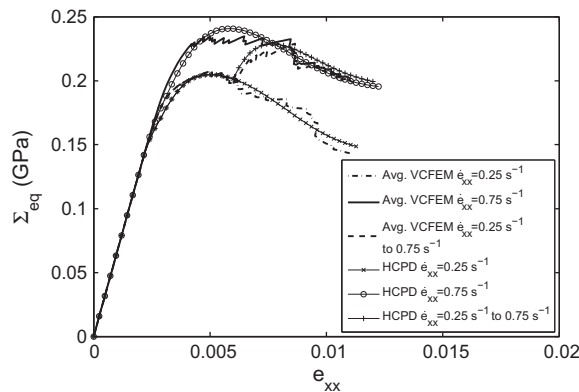


Fig. 15. Comparison of the macroscopic stress–strain responses by the rate-dependent HCPD model with LE-VCFEM simulations of RVE 1 in Fig. 5a for three different loading conditions.

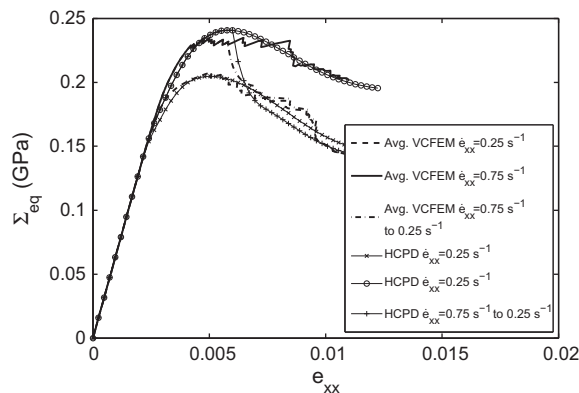


Fig. 16. Comparison of the macroscopic stress–strain responses by the rate-dependent HCPD model with LE-VCFEM simulations of RVE 1 in Fig. 5a for three different loading conditions.

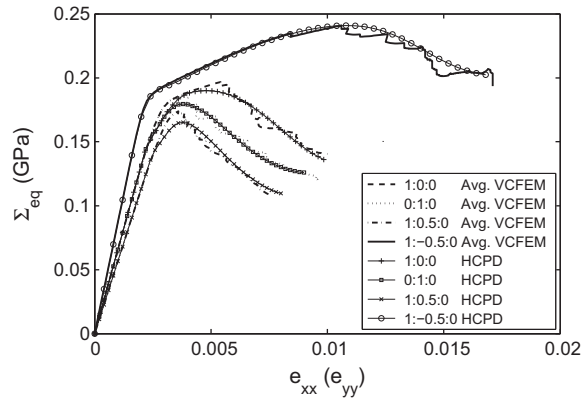


Fig. 17. Macroscopic stress–strain response of the HCPD model and the homogenized LE-VCFEM solution for RVE 1 in Fig. 5a subjected to different strain ratios $\bar{e}_{xx} : \bar{e}_{yy} : \bar{e}_{xy}$.

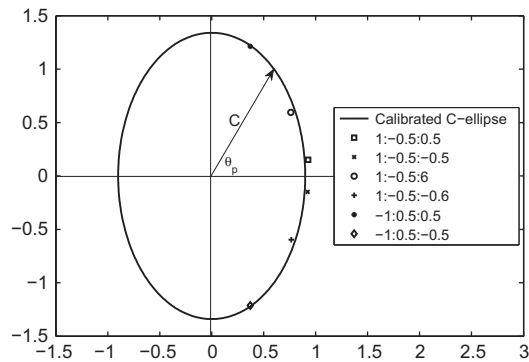


Fig. 18. Elliptical form of the parameter C obtained in Section 4.3 for RVE 1 along with the independently calibrated values of C for different strain ratios $\bar{e}_{xx} : \bar{e}_{yy} : \bar{e}_{xy}$ LE-VCFEM simulations.

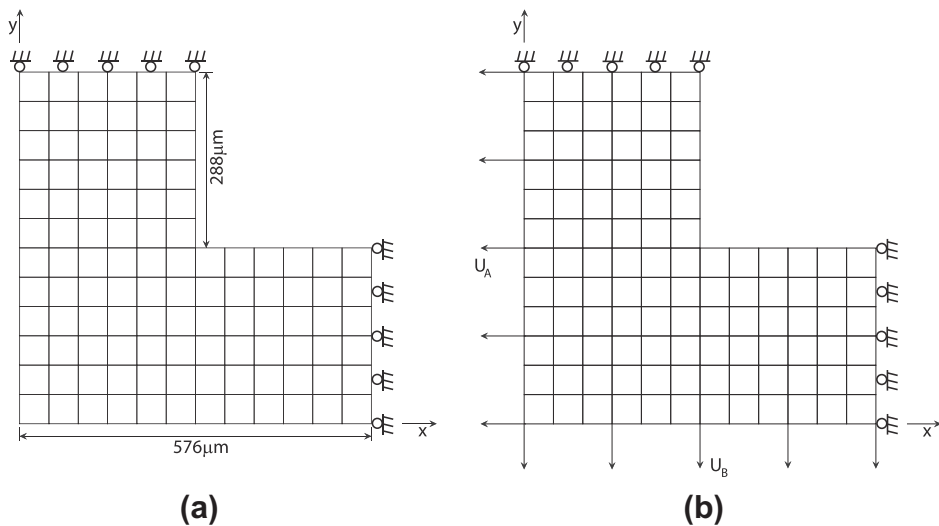


Fig. 19. (a) Geometry of the square plate with symmetry boundary conditions for macroscopic analyses, (b) two sets of boundary conditions are considered in addition to the symmetry boundary conditions: (1) uniaxial tensile loading in x -direction by prescribing displacement U_A at $x = 0$, (2) biaxial tensile loading by prescribing displacements U_A at $x = 0$ and U_B at $y = 0$.

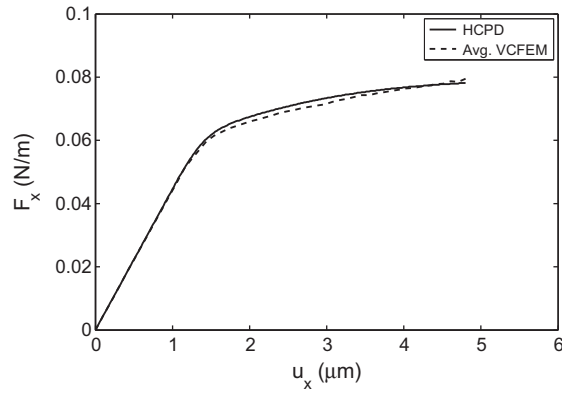


Fig. 20. Overall response of the structure in Fig. 19a subjected to an uniaxial tensile loading. The total reaction force F_x at the mid-section of the plate ($x = 576 \mu\text{m}$) is plotted as function of the applied displacement $u_x = |U_A|$.

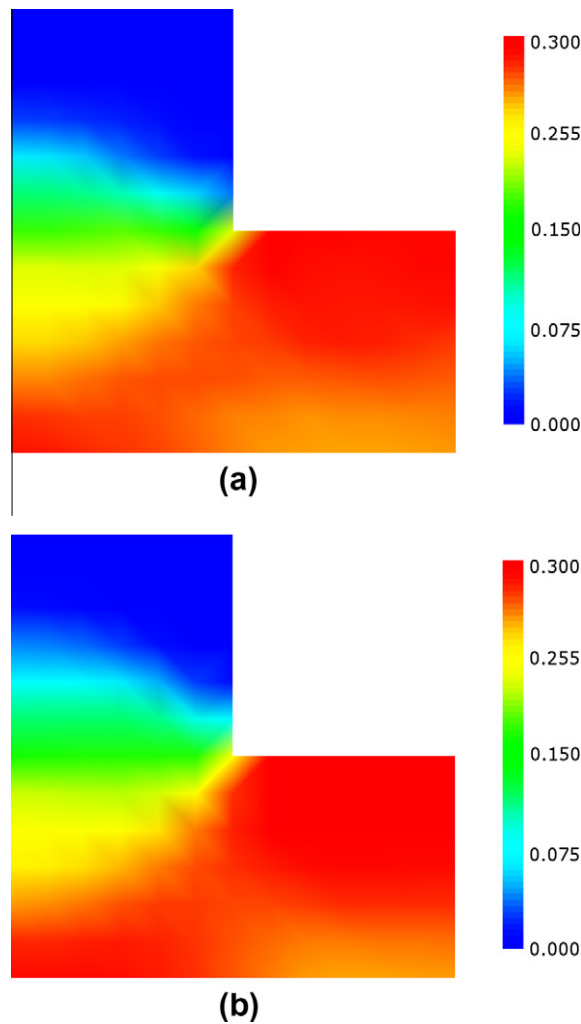


Fig. 21. Contour plots of macroscopic normal stress Σ_{xx} at an applied displacement $u_x = 4.800 \mu\text{m}$ obtained with: (a) micromechanical LE-VCFEM, and (b) rate-dependent HCPD model.

The final validation is performed to demonstrate the adequacy of the elliptical form in Fig. 12 for the nucleation anisotropy parameters A , B and C . A number of LE-VCFEM simulations of RVE 1 with different loading ratios ($\bar{e}_{xx} : \bar{e}_{yy} : \bar{e}_{xy} \neq 0$) are

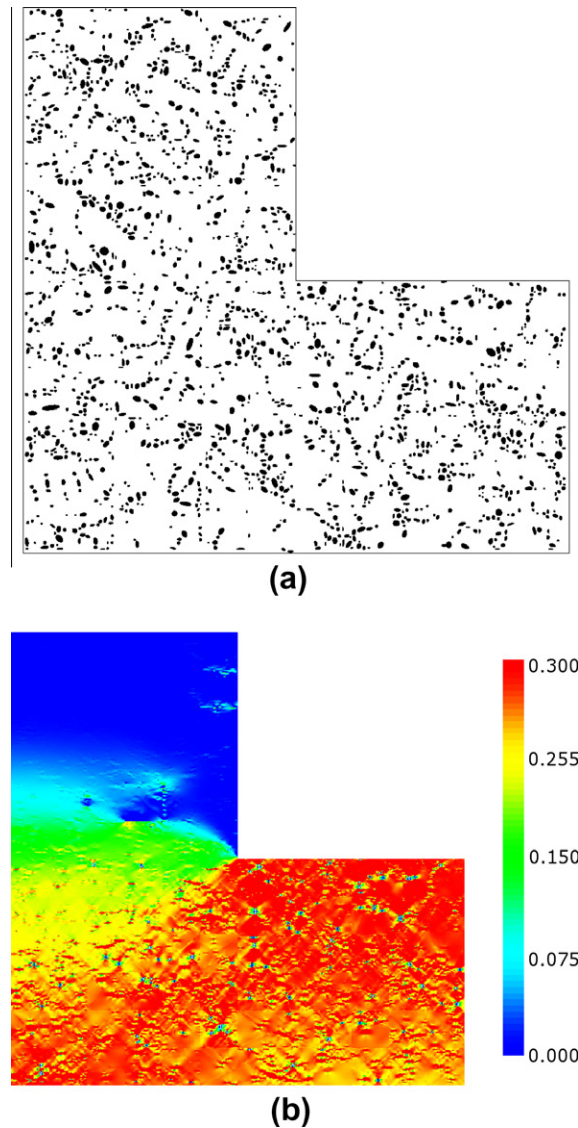


Fig. 22. (a) Micrograph taken from an actual W319 cast aluminum alloy imposed on the square plate. (b) Contour plot of microscopic normal stress σ_{xx} at an applied displacement $u_x = 4.800 \mu\text{m}$ obtained with the micromechanical LE-VCFEM.

performed. The value of parameter A is obtained from the ellipse, while the value of parameter C is independently calibrated from the homogenized micromechanical response. In Fig. 18 it is compared with the elliptical form calibrated in Section 4.3 for C . From the figure, it is seen that the independently calibrated values are very close to the elliptical form obtained from calibration. This validates the elliptical functional form used for describing the parameter C .

It is also important to note that LE-VCFEM simulations of RVE 1 for the two loading ratios $\bar{e}_{xx} : \bar{e}_{yy} : \bar{e}_{xy} = -1 : 0.5 : 0.5$ and $\bar{e}_{xx} : \bar{e}_{yy} : \bar{e}_{xy} = -1 : 0.5 : -0.5$ show no inclusion cracking. For these loading ratios, the values of A and C obtained from the ellipses using Eqs. 32 and 36 give a zero value for the area fraction of cracked inclusion ρ . Thus the anisotropy parameters are also capable of predicting loading conditions for which no inclusion cracking occurs.

6. Macroscopic analysis

In this section, macroscopic simulations are conducted with the HCPF model to study the nucleation and growth of voids in a square plate with a centered square hole. The plate is subjected to two different loading conditions. The geometrical dimensions of the plate are given in Fig. 19a. Only quarter of the plate is modeled with appropriate symmetry boundary conditions as illustrated in Fig. 19a. RVE 3 in Fig. 1b, taken from an actual cast aluminum alloy W319 microstructure as shown in Fig. 22a, is used for calibrating the rate-dependent HCPD model material parameters. Material parameters used for the LE-

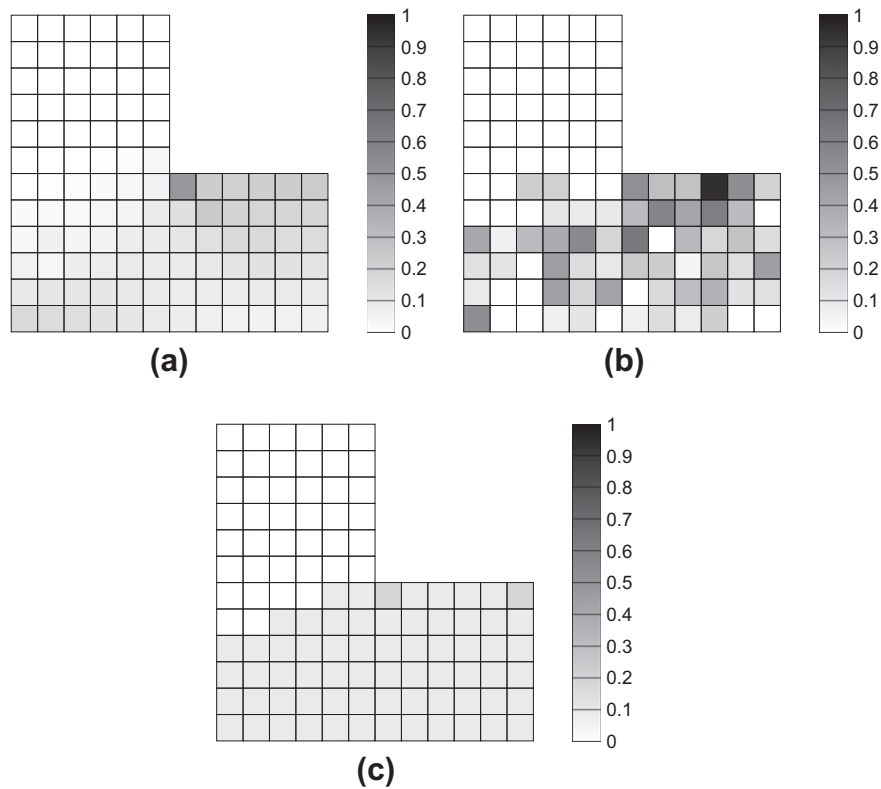


Fig. 23. Area fraction of cracked inclusions ρ at an applied displacement $u_x = 4.800 \mu\text{m}$ for the uniaxial loading condition (1) obtained with: (a) rate-dependent HCPD model, (b) LE-VCFEM simulation of the actual microstructure, and (c) LE-VCFEM simulation of a periodically repeated microstructure.

VCFEM simulations required are listed in Tables 1 and 2. The calibrated parameters associated with the GTN yield function Eq. (21) and void nucleation are given in Sections 4.2 and 4.3 respectively.

Two different loading conditions are considered for the macroscopic simulations. They are:

- (1) *Uniaxial tension*: In addition to the symmetry boundary conditions in Fig. 19a, a prescribed displacement $U_A = -4.800 \mu\text{m}$ is applied in the x -direction on the left edge ($x = 0$) of the plate as shown in Fig. 19b. The bottom of the plate ($y = 0$) is free of any prescribed displacement and no traction boundary conditions are applied. The total time of the simulation is set to $t = 0.0834 \text{ s}$.
- (2) *Biaxial tension*: In addition to the symmetry boundary conditions, a total prescribed displacement $U_A = U_B = -1.536 \mu\text{m}$ is applied in the x -direction at the left edge of the plate ($x = 0$) and in the y -direction at the bottom edge of the plate ($y = 0$). No traction boundary conditions are applied. The total time of simulation is set to $t = 0.0267 \text{ s}$.

Microscopic analyses using LE-VCFEM are also conducted for comparison. The actual microstructure of a cast aluminum alloy as observed from a micrograph is modeled with LE-VCFEM for the same loading conditions as for the macroscopic analyses. The overall response of the structure, obtained by the HCPD model and LE-VCFEM analyses are shown in Fig. 20 for the uniaxial tension loading condition (1). The total reaction force F_x in the mid-section of the plate ($x = 576 \mu\text{m}$) is plotted as a function of the applied displacement $u_x = |U_A|$. The two responses match very well. A comparison of the macroscopic normal stress Σ_{xx} at an applied displacement $U_A = -4.800 \mu\text{m}$ by the two models is also shown in Fig. 21. The corresponding contour plot of the microscopic normal stress σ_{xx} obtained with LE-VCFEM is shown in Fig. 22b. The very good match between these contour plots shows that the rate-dependent HCPD model is accurate in predicting macroscopic stresses in the structural component undergoing void nucleation by inclusion cracking and subsequent void growth.

To further validate the HCPD model and especially the void nucleation model, the area fraction of cracked inclusion ρ by the HCPD model in Fig. 23a is compared with that from micromechanics in Fig. 23b. An additional plot in Fig. 23c corresponds to the area fraction of cracked inclusions obtained with LE-VCFEM for a microstructure generated by periodic repetition of the RVE shown in Fig. 1b in each QUAD 4 element of Fig. 19. The HCPD model predictions agree well with that of LE-VCFEM for the repeated RVE. However, the results for the actual microstructure in Fig. 23b are somewhat different. The corresponding differences, defined as $\rho_{\text{diff}} = |\rho_{\text{HCPD}} - \rho_{\text{LE-VCFEM}}|$, for the different models are plotted in Fig. 24. The contour plots confirm good agreement between the HCPD model and the LE-VCFEM with a repeated microstructure. The same

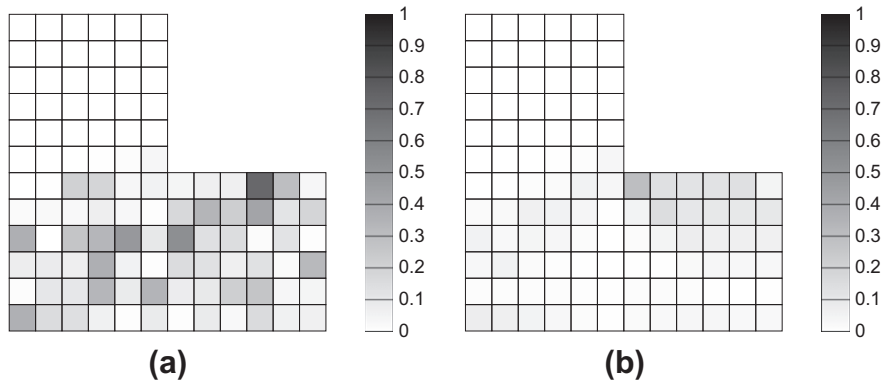


Fig. 24. Difference in area fraction of cracked inclusions ρ_{diff} at an applied displacement $u_x = 4.800 \mu\text{m}$ for the uniaxial loading condition (1) between the rate-dependent HCPD model and: (a) rate-dependent HCPD model, (b) LE-VCFEM simulation of the actual microstructure, and (c) LE-VCFEM simulation of a periodically repeated microstructure.

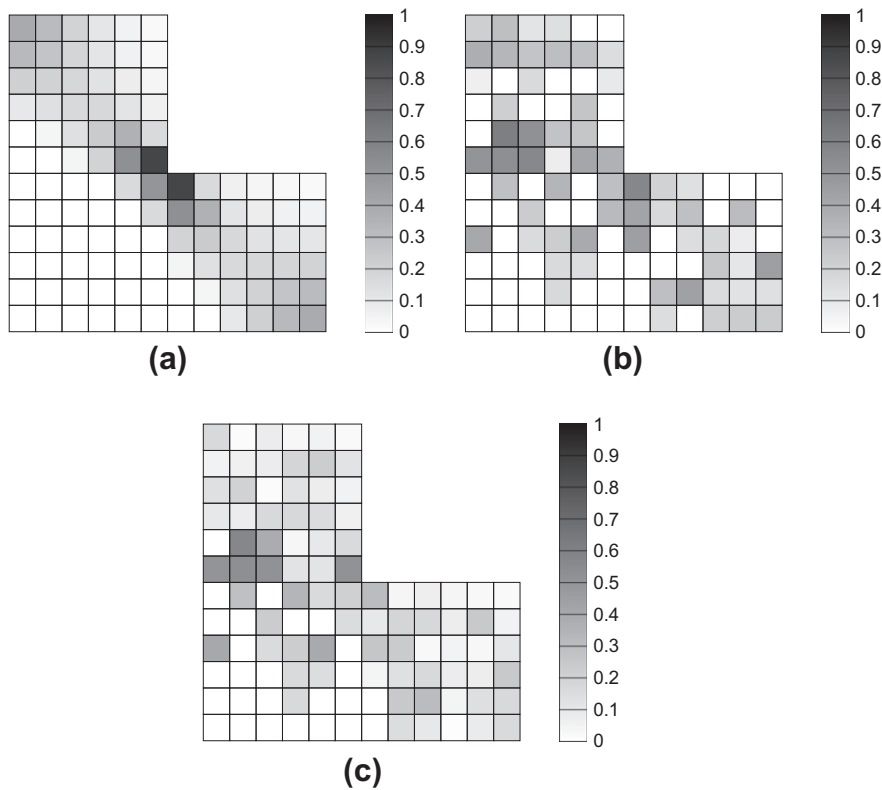


Fig. 25. Area fraction of cracked inclusions ρ at an applied displacement $u = 1.536 \mu\text{m}$ for the biaxial loading condition (2) obtained with: (a) HCPD model, (b) LE-VCFEM simulation of an actual microstructure, and (c) corresponding difference in ρ_{diff} .

observations are made for the biaxial loading condition (2). Fig. 25 shows the agreement in area fraction of cracked inclusions predicted by the two models.

The difference between the HCPD model and LE-VCFEM predictions for the actual microstructure in Figs. 24 and 25 is due to the local variations of the microstructure that cannot be captured by the HCPD model. The HCPD model is based on homogenization that uses periodicity. Since the nucleation model is primarily dependent on the size distribution of inclusions within the RVE, the difference between the HCPD model predictions and LE-VCFEM results for an actual microstructure must be related to the size of inclusions within the actual microstructure. To verify this assessment, an effective inclusion size is computed for the local microstructures within each *QUAD 4* element in the mesh of Fig. 19. This effective inclusion

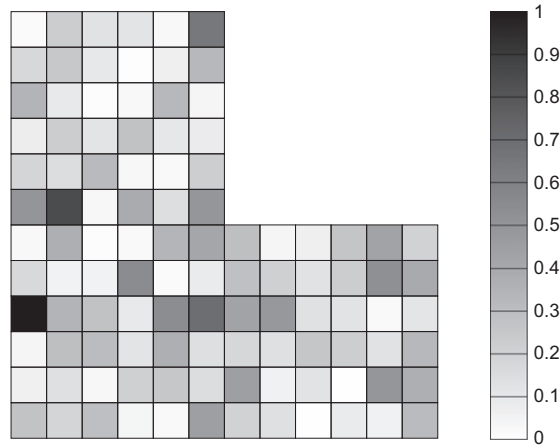


Fig. 26. Contour plot of d_{diff}^* showing the variation of the effective size d^* in the actual microstructure.

size d^* is a weighted size average defined as $(d^*)^2 = \frac{\sum w_i (d_i)^2}{\sum w_i}$, where $d_i = \sqrt{a_i b_i}$ is the size of the i th inclusion within the element (a_i and b_i are the major and minor axes). The weighting function $w_i = (d_i)^2$ is designed to give more weight to the larger inclusions that control damage nucleation in the microstructure. Fig. 26 shows the variation of the effective inclusion size within the actual microstructure, measured as a difference from the effective inclusion size as:

$$d_{\text{diff}}^* = \frac{|d^* - d_{\text{RVE}}^*|}{\max(|d^* - d_{\text{RVE}}^*|)} \quad (44)$$

where d_{diff}^* is normalized with respect to the largest difference found in all elements. It is seen that the regions corresponding to the largest differences between the HCPD model and LE-VCFEM predictions in Figs. 24 and 25 correlate well with large values of d_{diff}^* in Fig. 26.

7. Conclusions

An accurate and computationally efficient, rate-dependent homogenization based continuum plasticity damage (HCPD) model is developed for macroscopic analysis of ductile fracture in heterogeneous porous ductile materials in this paper. The rate-dependent HCPD model follows the structure of an anisotropic Gurson–Tvergaard–Needleman elasto-porous-plasticity model for ductile materials. Material anisotropy is determined by the morphology of the microstructure, as well as evolution of plastic deformation and damage. This anisotropy in plastic behavior is modeled with a set of anisotropy parameters, which evolve as a function of the plastic work. The entire rate-dependent HCPD model is expressed in an evolving material principal coordinate system, in which the material remains orthotropic throughout the deformation history. The model parameters are calibrated from the homogenization of microstructural variables obtained from LE-VCFEM simulations of the RVE.

The model also incorporates a unique rate-dependent void nucleation criterion that is capable of effectively simulating the loss of load carrying capacity of heterogeneous materials resulting from inclusion cracking and void growth. This model incorporates the effects of loading strain-rates on damage through the use of two parameters, viz. e_0 and m , which are functions of the local strain rate. The nucleation model also incorporates the anisotropy in damage evolution using three direction dependent parameters A , B and C . These are rate-independent and can be calibrated at any strain-rate. Numerical examples are conducted for a variety of loading conditions, such as different strain rates, instantaneously varying strain rates and different loading strain ratios. In all the cases, the rate-dependent HCPD model results show excellent agreement with the homogenized micromechanics results. Above all, the rate-dependent HCPD model has a huge advantage in terms of computational efficiency over explicit micromechanics simulations. The time taken to simulate both the rate-dependent HCPD model and the micromechanical LE-VCFEM model are compared to estimate the computational time advantage due to the HCPD model. The HCPD model shows a $1 \times 10^6 - 2 \times 10^6$ efficiency gain in computational time over LE-VCFEM, which makes the rate-dependent HCPD model a very effective tool in making macroscopic damage predictions.

Acknowledgments

This work has been supported by the National Science Foundation NSF Div Civil and Mechanical Systems Division through the GOALI Grant No. CMS-0308666 (Program Director: Dr. G. Paulino) and by the Department of Energy Aluminum Visions

Program through Grant No. A5997. This sponsorship is gratefully acknowledged. The authors are grateful to Drs. Steve Harris, John Allison, Xuming Su, and James Boileau of Ford Research Laboratory for invaluable discussions and for micrographs, samples and data used in this paper. Computer support by the Ohio Supercomputer Center through Grant PAS813-2 is also gratefully acknowledged.

References

- [1] Belytschko T, Liu W, Moran B. *Nonlinear finite elements for continua and structures*. England: Wiley; 2000.
- [2] Benssousan A, Lions J, Papanicolau G. *Asymptotic analysis for periodic structures*. Amsterdam: North Holland; 1978.
- [3] Benzerga A, Besson J, Pineau A. Anisotropic ductile fracture – Part II: Theory. *Acta Metall* 2004;52:4639–50.
- [4] Chu C, Needleman A. Void nucleation effects in biaxially stretched sheets. *J Engng Mater Tech* 1980;102:249–56.
- [5] Feyel F. A multilevel finite element method FE^2 to describe the response of highly non-linear structures using generalized continua. *Comput Meth Appl Mech Engng* 2003;192:3233–44.
- [6] Feyel F, Chaboche J. FE^2 multiscale approach for modelling the elastoviscoplastic behaviour of long fibre SiC/Ti composite materials. *Comput Meth Appl Mech Engng* 2000;183:309–30.
- [7] Garajeu M, Suquet P. Effective properties of porous ideally plastic or viscoplastic materials containing rigid particles. *J Mech Phys Solids* 1997;45:873–902.
- [8] Ghosh S. *Micromechanical analysis and multi-scale modeling using the Voronoi cell finite element method*. CRC Press, Taylor & Francis 2011.
- [9] Ghosh S, Bai J, Paquet D. Homogenization-based continuum plasticity-damage model for ductile failure of materials containing heterogeneities. *J Mech Phys Solids* 2009;57:1017–44.
- [10] Ghosh S, Bai J, Raghavan P. Concurrent multi-level model for damage evolution in microstructurally debonding composites. *Mech Mater* 2007;39:241–66.
- [11] Ghosh S, Kikuchi N. An arbitrary Lagrangian–Eulerian finite element method for large deformation analysis of elastic–viscoplastic solids. *Comput Meth Appl Mech Engng* 1991;86:127–88.
- [12] Ghosh S, Lee K, Moorthy S. Multiple scale analysis of heterogeneous elastic structures using homogenization theory and Voronoi cell finite element model. *Int J Solids Struct* 1995;32:27–62.
- [13] Ghosh S, Lee K, Moorthy S. Two scale analysis of heterogeneous elastic–plastic materials with asymptotic homogenization and Voronoi cell finite element model. *Comput Methods Appl Mech Engng* 1996;132:63–116.
- [14] Ghosh S, Lee K, Raghavan P. A multi-level computational model for multi-scale damage analysis in composite and porous materials. *Int J Solids Struct* 2001;38:2335–85.
- [15] Ghosh S, Valiveti DM, Harris SJ, Boileau J. A domain partitioning based pre-processor for multi-scale modeling of cast aluminum alloys. *Model Simulat Mater Sci Engng* 2006;14:1363–96.
- [16] Gurson A. Continuum theory of ductile rupture by void nucleation and growth: Part I – Yield criteria and flow rule for porous ductile media. *ASME J Engng Mater Tech* 1977;99:2–15.
- [17] Hashin Z. The elastic moduli of heterogeneous material. *J Appl Mech* 1962;29:143–50.
- [18] Hill R. A theory of yielding and plastic flow of anisotropic metals. *Proc Roy Soc A – Math Phys* 1948;193:281–97.
- [19] Hill R. On constitutive macro-variables for heterogeneous solids at finite strain. *Proc Roy Soc Lond* 1972;326:131–47.
- [20] Hu C, Ghosh S. Locally enhanced Voronoi cell finite element model (LE-VCFEM) for simulating evolving fracture in ductile microstructures containing inclusions. *Int J Numer Meth Engng* 2008;76(12):1955–92.
- [21] Hu C, Ghosh S. Locally enhanced Voronoi Cell finite element model (LE-VCFEM) for simulating evolving fracture in ductile microstructures containing inclusions. *Int J Numer Meth Engng* 2008;76:1955–92.
- [22] Moorthy S, Ghosh S. A Voronoi cell finite element model for particle cracking in elastic–plastic composite materials. *Comput Method Appl Mech Engng* 1998;151:377–400.
- [23] Moorthy S, Ghosh S. Adaptivity and convergence in the Voronoi cell finite element model for analyzing heterogeneous materials. *Comput Method Appl Mech Engng* 2000;185:37–74.
- [24] Mori T, Tanaka K. Average stress in the matrix and average elastic energy of materials with misfitting inclusions. *Acta Metall* 1973;21:571–4.
- [25] Paquet D, Dondeti P, Ghosh S. Dual-stage nested homogenization for rate-dependent anisotropic elasto-plasticity model of dendritic cast aluminum alloys. *Int J Plast* 2011;27:1677–701.
- [26] Paquet D, Ghosh S. Microstructural effects on ductile fracture in heterogeneous materials. Part I: Sensitivity analysis with LE-VCFEM. *Engng Fract Mech* 2011;78:205–25.
- [27] Paquet D, Ghosh S. Microstructural effects on ductile fracture in heterogeneous materials. Part II: Application to cast aluminum microstructures. *Engng Fract Mech* 2011;78:226–33.
- [28] Perzyna P. Fundamental problems in viscoplasticity. *Adv Appl Mech* 1966;9:243–377.
- [29] Ponte Castaneda P, Suquet P. Nonlinear composites. *Adv Appl Mech* 1998;34:171–302.
- [30] Raghavan P, Ghosh S. A continuum damage mechanics model for unidirectional composites undergoing interfacial debonding. *Mech Mater* 2005;37:955–79.
- [31] Sanchez-Palencia E. *Non-homogeneous media and vibration theory*. Lecture notes in physics. Berlin (Heidelberg): Springer-Verlag; 1980.
- [32] Swaminathan S, Ghosh S. Statistically equivalent representative volume elements for unidirectional composite microstructures: Part II – With damage. *J Compos Mater* 2006;40:605–21.
- [33] Swaminathan S, Ghosh S, Pagano N. Statistically equivalent representative volume elements for unidirectional composite microstructures: Part I – Without damage. *J Compos Mater* 2006;40:583–604.
- [34] Tvergaard V. On localization in ductile materials containing voids. *Int J Fract* 1982;18:237–51.
- [35] Tvergaard V, Needleman A. Analysis of cup-cone fracture in round tensile bar. *Acta Metall* 1984;32:157–69.
- [36] Wang D, Pan J, Liu S. An anisotropic Gurson yield criterion for porous ductile sheet metals with planar anisotropy. *Int J Damage Mech* 2004;13:7–33.
- [37] Wang Q. Microstructural effects on the tensile and fracture behaviour of aluminum casting alloys A356/357. *Metall Mater Trans Mech A* 2003;34:2887–99.
- [38] Willis J. Variational and related methods for the overall properties of composites. *Adv Appl Mech* 1981;21:1–78.